Internal structure of the San Jacinto fault zone at Blackburn Saddle from seismic data of a linear array

Pieter-Ewald Share,[1] Yehuda Ben-Zion,[1] Zachary E. Ross,[2] Hongrui Qiu[1] and Frank L. Vernon[3]

[1]*Department of Earth Sciences, University of Southern California, Los Angeles, CA 90089, USA. E-mail: pshare@usc.edu*
[2]*Seismological Laboratory, California Institute of Technology, Pasadena, CA 91125, USA*
[3]*Scripps Institution of Oceanography, University of California San Diego, La Jolla, CA 92093, USA*

SUMMARY

Local and teleseismic earthquake waveforms recorded by a 180-m-long linear array (BB) with seven seismometers crossing the Clark fault of the San Jacinto fault zone northwest of Anza are used to image a deep bimaterial interface and core damage structure of the fault. Delay times of *P* waves across the array indicate an increase in slowness from the southwest most (BB01) to the northeast most (BB07) station. Automatic algorithms combined with visual inspection and additional analyses are used to identify local events generating fault zone head and trapped waves. The observed fault zone head waves imply that the Clark fault in the area is a sharp bimaterial interface, with lower seismic velocity on the southwest side. The moveout between the head and direct *P* arrivals for events within ∼40 km epicentral distance indicates an average velocity contrast across the fault over that section and the top 20 km of 3.2 per cent. A constant moveout for events beyond ∼40 km to the southeast is due to off-fault locations of these events or because the imaged deep bimaterial interface is discontinuous or ends at that distance. The lack of head waves from events beyond ∼20 km to the northwest is associated with structural complexity near the Hemet stepover. Events located in a broad region generate fault zone trapped waves at stations BB04–BB07. Waveform inversions indicate that the most likely parameters of the trapping structure are width of ∼200 m, *S* velocity reduction of 30–40 per cent with respect to the bounding blocks, *Q* value of 10–20 and depth of ∼3.5 km. The trapping structure and zone with largest slowness are on the northeast side of the fault. The observed sense of velocity contrast and asymmetric damage across the fault suggest preferred rupture direction of earthquakes to the northwest. This inference is consistent with results of other geological and seismological studies.

Key words: Earthquake dynamics; Body waves; Interface waves; Guided waves; Rheology and friction of fault zones; Continental tectonics: strike-slip and transform.

1 INTRODUCTION

The 230-km-long San Jacinto fault zone (SJFZ) is the most seismically active fault zone in southern California (Hauksson *et al.* 2012) and accommodates a large portion of the plate boundary motion in the region (Johnson *et al.*1994; Fialko 2006; Lindsey *et al.* 2014). Extensive palaeoseismic work indicates that the SJFZ has repeatedly produced large ($M_W > 7.0$) earthquakes in the past 4000 yr (Rockwell *et al.* 2015, and references therein). Variations of lithological units and geometrical complexities (e.g. Sharp 1967) produce non-uniform distribution of strain and seismicity along the length of the fault (Sanders & Kanamori 1984; Sanders & Magistrale 1997, Hauksson *et al.* 2012). Recent tomographic studies (Allam & Ben-Zion 2012; Allam *et al.* 2014a; Zigone *et al.* 2015)

imaged with nominal resolution of 1–2 km large-scale variations of seismic velocities across the fault and significant damage zones at different locations. Internal structural components of the SJFZ have been studied using various seismic arrays that cross the fault at different locations (e.g. Li & Vernon 2001; Lewis *et al.* 2005; Yang *et al.* 2014; Ben-Zion *et al.* 2015; Li *et al.* 2015; Hillers *et al.* 2016), along with geological mapping of rock damage and analysis of geomorphologic signals (Dor *et al.* 2006; Wechsler *et al.* 2009).

In this study we use several seismological techniques to clarify internal components of the SJFZ at Blackburn Saddle northwest of Anza. The study area is at the head of Blackburn Canyon near the northwestern end of the longest continuous strand of the SJFZ, the Clark Fault (Sharp 1967). The site ruptured during two large earthquakes in the last 250 yr, the *M* 7.2–7.5 1800 event
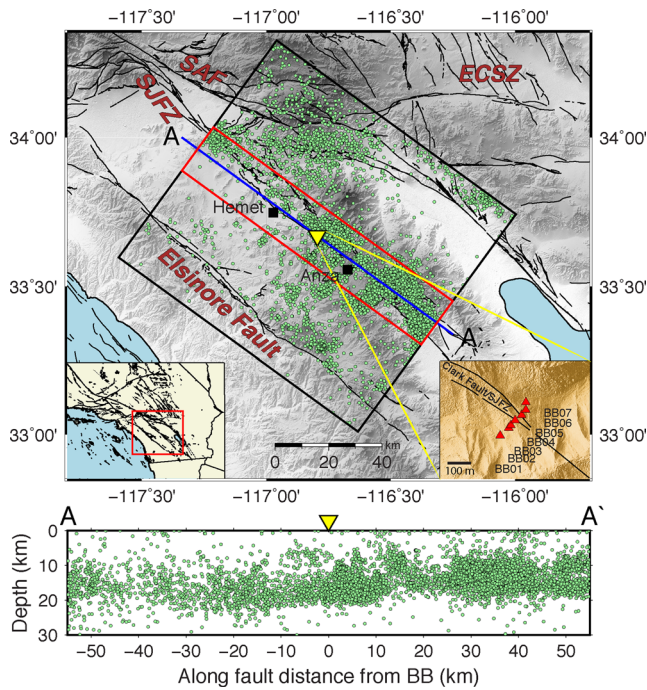
Figure 1. Toppanel: the study region (110 km by 100 km black box) centred on the Clark fault in the San Jacinto fault zone (SJFZ). The San Andreas (SAF), Elsinore faults and Eastern California shear zone (ECSZ) are marked. Waveforms from events (light green circles) within the black box are inspected for FZTW. Events within the red rectangle (110 km by 20 km) are used for delay time and FZHW studies. The yellow triangle shows the location of the BB array. The black squares mark the towns of Anza and Hemet. Bottom panel: A depth section of events projected along the profile A–A′ on top.

(Salisbury *et al.* 2012) and the *M* 6.8 1918 earthquake (Sanders & Kanamori 1984). The analyses employ earthquake waveforms recorded for about 1.5 yr by a linear seismic array (BB array, Fig. 1 bottom right inset) across the Clark fault in the study area. We use delay times of *P* arrivals across the array, fault zone head waves (FZHW) and fault zone trapped waves (FZTW) to image properties of the fault damage zone and bimaterial fault interface. We focus on these structural components because they contain information on likely properties of past and future earthquake ruptures and associated ground motion (e.g. Andrews & Ben-Zion 1997; Dor *et al.* 2006, 2008; Brietzke *et al.* 2009; Shlomai & Fineberg 2016).

FZHW propagate along a fault bimaterial interface with the velocity and motion polarity of the body waves on the faster side of the interface. These phases are analogous to *Pn* head waves in horizontally layered media, and they arrive at near-fault stations on the slower side of the fault before the direct body waves. FZHW provide the highest resolution tool for imaging the existence and properties of bimaterial fault interfaces (e.g. Ben-Zion *et al.* 1992; McGuire & Ben-Zion 2005). On the other hand, misidentification of FZHW as direct arrivals can introduce biases and errors into derived velocity structures, earthquake locations and fault plane solutions (e.g. McNally & McEvilly 1977; Oppenheimer *et al.* 1988; Bennington *et al.* 2013). FZTW are slow seismic energy associated with resonance modes within low-velocity fault zone layers. For the antiplane *S* case they are analogous to surface Love waves of a horizontally layered structure, while for the *P* case they are analogous to surface Raleigh waves or leaky modes (e.g. Ben-Zion

Table 1. Locations of the seven BB stations.

Station name	Latitude (°)	Longitude (°)	Elevation (m)
BB01	33.66871	−116.79584	1173
BB02	33.66897	−116.79544	1167
BB03	33.66914	−116.79528	1165
BB04	33.66927	−116.79511	1165
BB05	33.66946	−116.79480	1169
BB06	33.66967	−116.79462	1169
BB07	33.66999	−116.79456	1180

& Aki 1990; Ellsworth & Malin 2011). The generation of FZTW requires a sufficiently coherent zone of damaged rocks that can act as a waveguide (e.g. Igel *et al.* 1997; Jahnke *et al.* 2002). These and other less coherent parts of the fault damage zone also produce delay time of direct *P* and *S* waves propagating through the fault zone structure (e.g. Lewis & Ben-Zion 2010; Yang *et al.* 2014; Qiu *et al.* 2017).

In the next section we provide more detail on the array stations and data. The analysis techniques and results are described in Section 3 using four subsections. The first two subsections contain information on identification of *P* arrivals from teleseismic and local earthquakes, and related calculations of delay times across the array. The latter two subsections describe identification and analyses of FZHW and FZTW. The results are summarized and discussed in the last section of the paper.

2 INSTRUMENTATION AND DATA

The BB array is part of a PASSCAL deployment (YN) within and around the SJFZ (Vernon & Ben-Zion 2010). The array comprises of 7 Guralp CMG-40T-1 short period three-component sensors installed ∼30 m apart (locations in Table 1). The array is orientated normal to the surface trace of the Clark Fault and the middle sensor (BB04) is installed on top of the surface trace of the fault (Fig. 1 bottom right inset). The instruments measure ground velocity and have a flat frequency amplitude response between 1 and 100 Hz with a sampling rate of 200 Hz. Recording started on 2012 November 18 and ended on 2014 April 26.

A catalogue of seismicity up to 2013 for the SJFZ region (White *et al.* 2016) is used to extract local event waveforms from continuous BB recordings. The catalogue utilizes the Anza network, nearby stations of the Southern California Seismic Network and stations from several local deployments. We extract 80 s long waveforms for events occurring from 2012 November 18 to 2013 December 31, 10 s before and 70 s after the origin times reported in the catalogue. In total, 10 603 of these events are located within a 110 km by 100 km box centred on the array and aligned with the Clark Fault. *S* waveforms generated by the 10 603 events are analysed in the FZTW study (Fig. 1). *P* arrivals and waveforms from 8216 events contained in a smaller region (110 km by 20 km, red box in Fig. 1) are analysed in the delay time and FZHW studies.

P waveforms corresponding to all *M* > 5 teleseismic earthquakes (within 30°–100°) contained in the Southern California Earthquake Data Center (SCEDC 2013) that occurred during the study period are extracted from BB data in 30 s windows. A subset of 79 high quality events with sufficiently high signal-to-noise ratio is retained for further analysis (Fig. 2a).
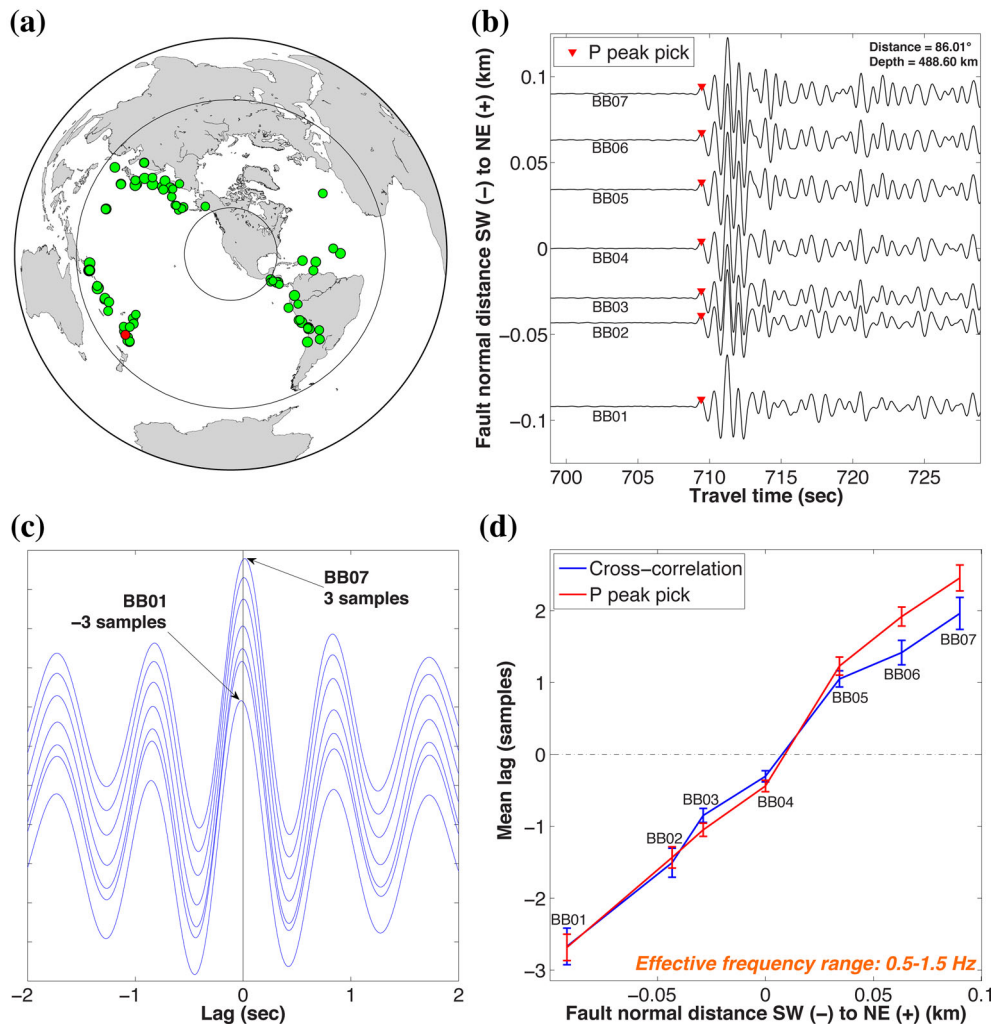
Figure 2. Relative delay time results based on teleseismic *P* waves. (a) Locations of 79 events used in the study with the red circle representing an example event. (b) Velocity waveforms (vertical component) of the example event normalized by the absolute maximum of BB01 and aligned relative to the event origin time. Red triangles depict manual *P* picks. (c) Cross-correlation functions between each BB trace and a template trace (see text for calculation of template, positive lag = delayed arrival). (d) Average relative delay of all events based on manual picking and cross-correlation. Effective frequency range refers to the dominant frequencies of teleseismic *P* waves analysed here.

3 METHODS AND RESULTS

3.1 Teleseismic earthquake delay time

The primary factors that contribute to *P*-wave pick time variations between BB stations are incorrect identification of *P*-wave arrivals, variations due to propagation paths to different stations and variations in local *P* velocity structure. The performed delay time analysis provides statistical information on *P* arrival times determined from waveforms generated by numerous events, with the aim of constraining the local velocity structure.

In the case of teleseismic events, the first step consists of accurately determining *P* arrival time differences between stations. This is done in two ways. Firstly, for a given event the first *P* maxima/minima coherent across the array are picked and designated *P* arrivals (*P* peak picks in Fig. 2b). They are more readily identified than the first arriving *P* energy because the latter in almost all cases is low in amplitude and comparable to the noise level. Secondly, relative time delays between stations are obtained using cross-correlation of the 30 s waveforms (Fig. 2c). If the first maximum/minimum has large amplitude and is coherent while the

trailing waveform is incoherent across the array, then *P* peak pick differences give the best estimates of relative arrival times. In contrast, if the first maximum/minimum has low amplitude (more prone to be affected by noise) but entire waveforms are coherent between stations, then cross-correlation is the best method to estimate relative arrival times. The two methods jointly provide a robust way of estimating relative times between stations for a variety of teleseismic *P* waveforms.

The second step encompasses minimizing time variations due to different propagation paths. Arrival times at different stations in the absence of shallow lateral velocity changes and topography are first approximated using TauP (Crotwell *et al.* 1999) and the IASP91 model. Although the BB array is located ∼1 km above sea level, topography varies little within the array (largest difference is 15 m, Table 1). Therefore, constant horizontal slowness can be assumed and the relative arrival times at the average elevation across the array are equal to times predicted using TauP. For manual *P* picks the predicted arrival times are removed from picked arrival times for each event. Prior to cross-correlation the same predicted arrival times are used to appropriately shift the time-series.
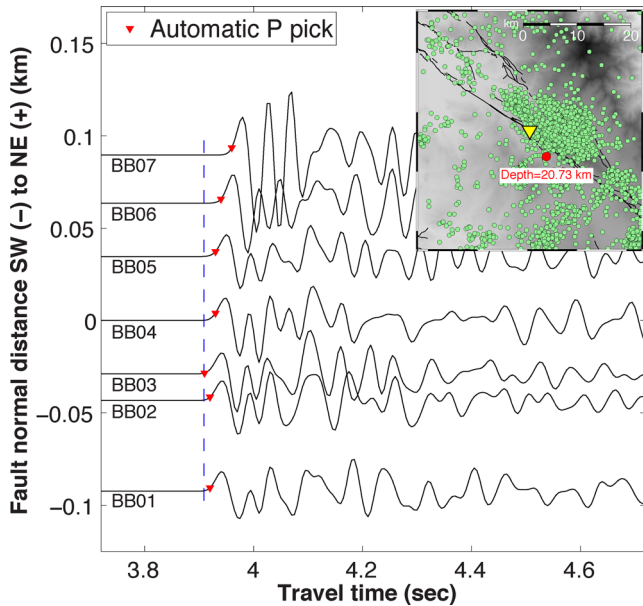
Figure 3. Automatic *P* picks (red triangles) made on velocity waveforms (vertical component) generated by an example event with hypocentre ~20 km away (location in inset). Waveforms are normalized by BB01 and aligned relative to the event origin time. The dashed blue line is aligned with the pick at BB03 and highlights the arrival time differences between stations.

During the final step relative delays are computed and velocity structure is inferred from the delays. In the case of manual picks, the average of the remaining times for each event is subtracted to produce relative delay times. Next, means and standard errors of the 79 relative delays at each station are computed (red curve in Fig. 2d). In the case of cross-correlation any trend is removed from the data and a bandpass filter between 0.2 and 2 Hz is applied. A template is then created for each event by summing the seismograms across the array. Next, a cross-correlation function is calculated and used to measure the relative delay time from the peak correlation lag. Similar to manual picking, means and standard errors of the 79 relative delays at each station are computed (blue curve in Fig. 2d). Both results using manual picking and cross-correlation show a gradual increase in relative delay from BB01 to BB07, suggesting an increase in subsurface slowness from southwest to northeast. The observed gradual increase in slowness reflects the relatively low dominant frequencies of the teleseismic *P* waves (0.5–1.5 Hz).

3.2 Local earthquake delay time

We perform a similar analysis using local earthquakes with a slightly modified methodology. First, we process the early *P* waveforms for all (>10 000) earthquakes with an automatic algorithm (Ross & Ben-Zion 2014). The algorithm uses short-term average to long-term average detectors together with kurtosis- and skewness-based detectors to identify and pick the onset times of *P* waves (Fig. 3), and FZHW if present. To avoid ambiguity between FZHW and direct *P* phases, if a FZHW pick is made at any BB station for a given event, then that event is discarded for the delay time analysis. For all remaining events, outlier *P* picks are systematically removed through the application of the following steps:

(1) We discard *P* wave picks more than 1 s off from predicted arrival times, using an average 1-D model discretized in 1 km layers
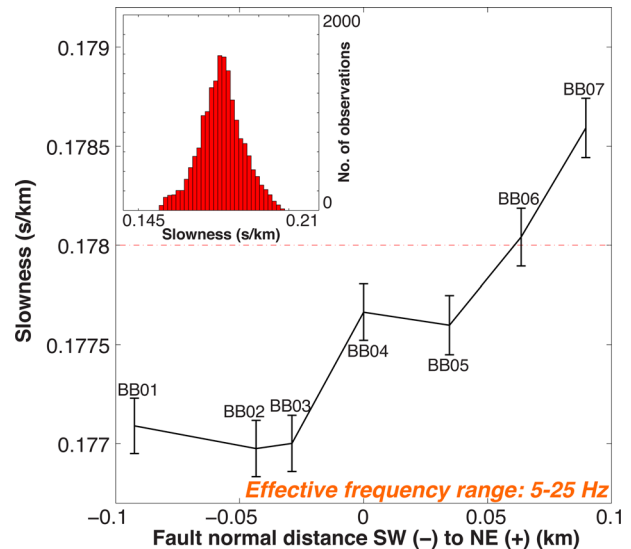

Figure 4. Delay time results derived from automatic *P* picks of local arrivals. Slowness values are calculated from arrival times (see text) and a mean and standard error of slowness is calculated at each station individually (black curve and error bars) using 2503, 2458, 2574, 2550, 2495, 2550 and 2462 data points for BB01 to BB07, respectively. Effective frequency range refers to the dominant frequencies of local *P* arrivals analysed here. Top left inset shows the distribution of this data and the horizontal dashed line in the main plot equals the peak in the distribution.

based on the 3-D tomographic results of Allam & Ben-Zion (2012) for the region.

(2) Each observed travel time is normalized by the theoretical ray length computed from the 1-D model to obtain an average slowness. This minimizes differences in travel times due to station separation and homogenizes travel times associated with different event hypocentres. We then discard picks which have slowness values outside a reasonable range (0.13–0.22 s km^{-1}) bounded by the corresponding maximum and minimum velocities (7.73 and 4.57 km s^{-1}) of the 1-D model.

(3) Events with slowness values at fewer than four stations are removed to focus on observations associated with most of the array stations.

(4) A final round of outlier removal is applied using statistical inner and outer fencing. That is, a given slowness value s is considered an outlier and removed if $s <$ Q1-1.5(Q3-Q1) or $s >$ Q3+1.5(Q3-Q1), where Q1 and Q3 are the slowness values nearest to the first and the third quartile, respectively.

The picking algorithm initially produced 37 206 *P* and 2033 FZHW picks for 6573 and 758 events, respectively. After completing the aforementioned steps, 17 592 *P* picks from 2777 events remained (histogram in Fig. 4). Fig. 4 displays the mean slowness and associated standard errors for the BB array. Similar to the teleseismic results, the largest subsurface slowness is observed for BB07. The increase in slowness from BB01 to BB07 is not as smooth as in Fig. 2d, reflecting the higher dominant frequencies of local *P* waves (5–25 Hz) compared to the teleseismic data and associated higher sensitivity to small-scale heterogeneities. Following an outlier exclusion process, a significant amount of variability still exists for each station (large error bars in Fig. 4). While picking errors can account for some of this, most of the variability is likely the result of 3-D structure outside the fault zone. One way to more appropriately deal with this is by comparing relative slowness values between stations, rather than absolute slowness. Subsequently, for each event
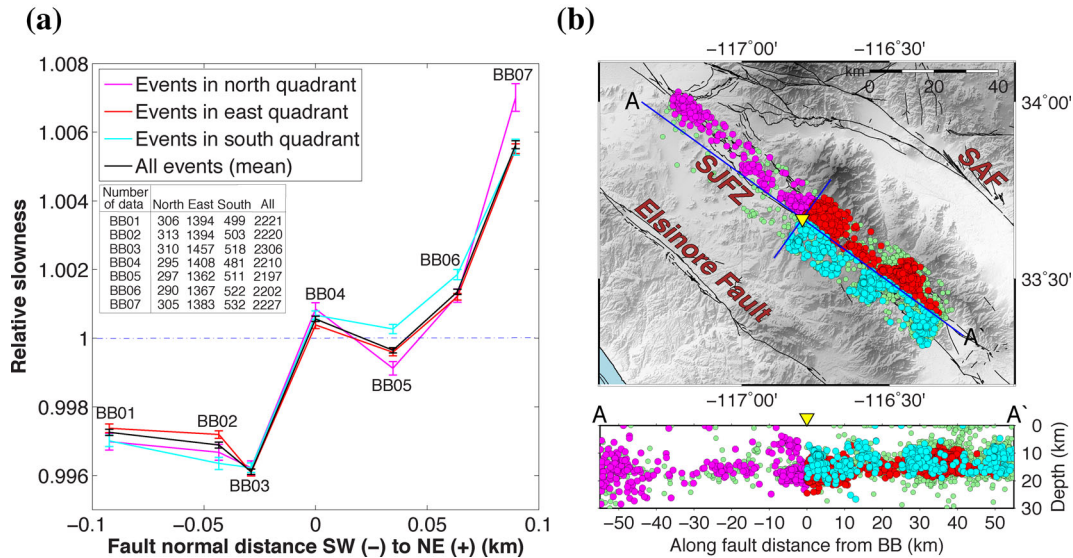
Figure 5. Relative delay time results of local arrivals. (a) Estimates based on all events (black curve) are compared to those using events north (magenta), east (red) and south (cyan) of the array. (b) (Top) Locations of north (magenta), east (red) and south (cyan) event subsets. Yellow triangle represents the array location. (Bottom) A depth section of events projected along the profile A–A′ on top.

we estimate the relative slowness by dividing each non-zero slowness value by the mean slowness across the array of that event. Then we calculate the mean and standard error of relative slowness at each station individually. These calculations show (Fig. 5a, black line) that BB07 has larger relative slowness compared to BB01 and the error bar for each station calculation is significantly reduced. In summary, rays propagating to BB07 sample on average structure that is 0.9–1.2 per cent slower than rays propagating to BB01.

To check whether the results are independent of azimuth, events are partitioned into north, east and south blocks (Fig. 5b) and for each corresponding dataset the mean and standard error are computed per station. Same computations are not made for events located west of the array due to a lack in seismicity. The relative slowness of each subset of data is almost identical to the relative slowness calculated from all data at every station (Fig. 5a). This indicates that the general increase in slowness from BB01 to BB07 is associated with local structure and effects of 3-D variations outside the fault zone are not significantly present in the relative slowness data.

3.3 Fault zone head waves

3.3.1 Methodology

FZHW are critically refracted emergent phases that travel along a fault bimaterial interface with the velocity and motion polarity of the faster medium (Ben-Zion, 1989, 1990). They arrive before the impulsive direct *P* waves at locations on the slower medium with normal distance to the fault less than a critical distance x_c given by

$$x_c = r \cdot \tan\left(\cos^{-1}\left(\alpha_s/\alpha_f\right)\right), \tag{1}$$

where *r* is the propagation distance along the fault (both along-strike and up-dip direction) and α_s, α_f are the average *P* wave velocities of the slower and faster media, respectively (Ben-Zion 1989). For events with focal mechanisms coinciding with the fault, FZHW and trailing direct *P* waves have opposite first motion polarities (Ben-Zion & Malin 1991; Ross & Ben-Zion 2014). Also, FZHW are radiated from the fault and have horizontal particle motion (HPM)

with a significant fault-normal component (Bulut *et al.* 2012; Allam *et al.* 2014b; Share & Ben-Zion 2016). In contrast, HPM of direct *P* waves points in the epicentre direction. The differential time Δt between FZHW and direct *P* waves increases with propagation distance along the fault and is related to the average velocity α across the fault by (Ben-Zion & Malin 1991):

$$\Delta t \approx r \cdot \Delta\alpha/\alpha^2, \tag{2}$$

where $\Delta\alpha$ is the differential *P*-wave velocity. Also, Δt decreases with increasing normal distance from the fault to zero at the critical distance x_c.

3.3.2 Results

Using the criteria in Section 3.3.1 we focus on determining which of the events previously flagged by the automatic detector (and discarded in Section 3.2) produce FZHW. The detector flags *P* waveforms with an emergent phase followed by an impulsive arrival with a time separation between a minimum value (0.065 s representing the width of a narrow *P* wave wiggle) and a maximum value that depends on hypocentral distance (e.g. 0.8 s over a distance of 40 km). The latter is calculated assuming a faster side velocity of 5.5 km s^{-1} and a velocity contrast of 10 per cent based on the tomographic results of Allam & Ben-Zion (2012). We do not require polarity reversal between FZHW and direct *P* waves because of the mixed complex focal mechanisms for events in the region (Bailey *et al.* 2010).

Arrivals from flagged events recorded at different stations are visually compared to remove erroneous picks such as emergent early phases similar to the noise. For each event we also inspect the waveforms recorded at two reference stations that are part of the regional network and are close to the BB array (BCCC and RHIL, Fig. 6). If emergent first arrivals are flagged at both reference stations, those emergent phases are not FZHW (since head waves exist only on one side of a fault bimaterial interface) and the event is discarded. We then search for events in the catalogue within 10 km of the remaining events and examine them visually for possible additional FZHW phases. The automatic detector uses settings designed to
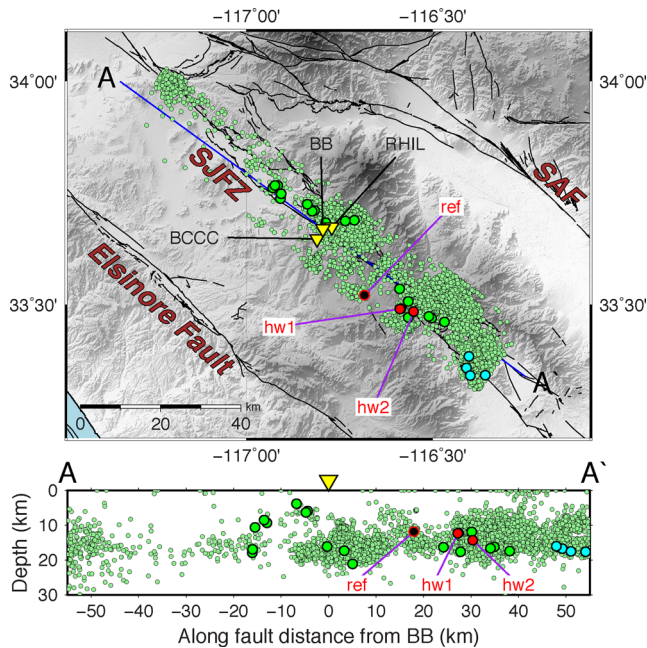
Figure 6. Stations and events used in FZHW analysis. Toppanel: waveforms from events (all circles) 10 km from the fault recorded at the array and reference stations BCCC and RHIL 3 km southwest and 2 km northeast of the fault, respectively, are analysed for FZHW. A total of 24 events (large green, red and light blue circles) producing FZHW at the array and station BCCC are identified. Figs 7 and 8 contain waveforms and analysis from one event (ref, large red black-filled circle) with no FZHW and two events generating FZHW (hw1 and hw2, large red circles). Bottompanel: a depth section of events projected along the profile A–A′ on top. Yellow triangle represents the location of the array.

primarily minimize false detections, at the cost of reducing detection of events with FZHW, and performing this additional search helps to make up for this shortcoming. The identification steps produces 49 events generating candidate FZHW at all BB stations and only reference station BCCC for events with large enough propagation distance along the fault (Fig. 7, top and middle panels). FZHW picks for these events are adjusted to where associated emergent phases begin to rise above the noise level (Fig. 7, top and middle panels).

Next we apply HPM analysis on the early *P* waveforms that are detrended, filtered using a 1–30 Hz one-pass Butterworth filter and integrated to displacement. Similar to previous studies (e.g. Allam *et al.* 2014b; Najdahmadi *et al.* 2016), we examine HPM in displacement seismograms with consecutive moving time windows of length 0.1 s (20 samples) that overlap by 1 sample. For each window, all three components of motion are combined in a 20×3 matrix, the covariance of the matrix is computed (Bulut *et al.* 2012) and the largest eigenvalue and eigenvector of the covariance matrix (major axis of the polarization ellipse) are obtained. We then test to see if the azimuth of the largest eigenvector for windows starting at the FZHW and direct *P* picks point, respectively, towards the fault and the epicentre direction. The results indicate that for the 49 candidate events there is considerable variability in the particle motion directions. The azimuths calculated from windows containing direct *P* waves do not consistently point to the epicentres and azimuths calculated for the same event often vary up to ∼60° between BB stations. Similar variations are observed for the head waves. The variability in HPM is likely caused by the complex structure be-
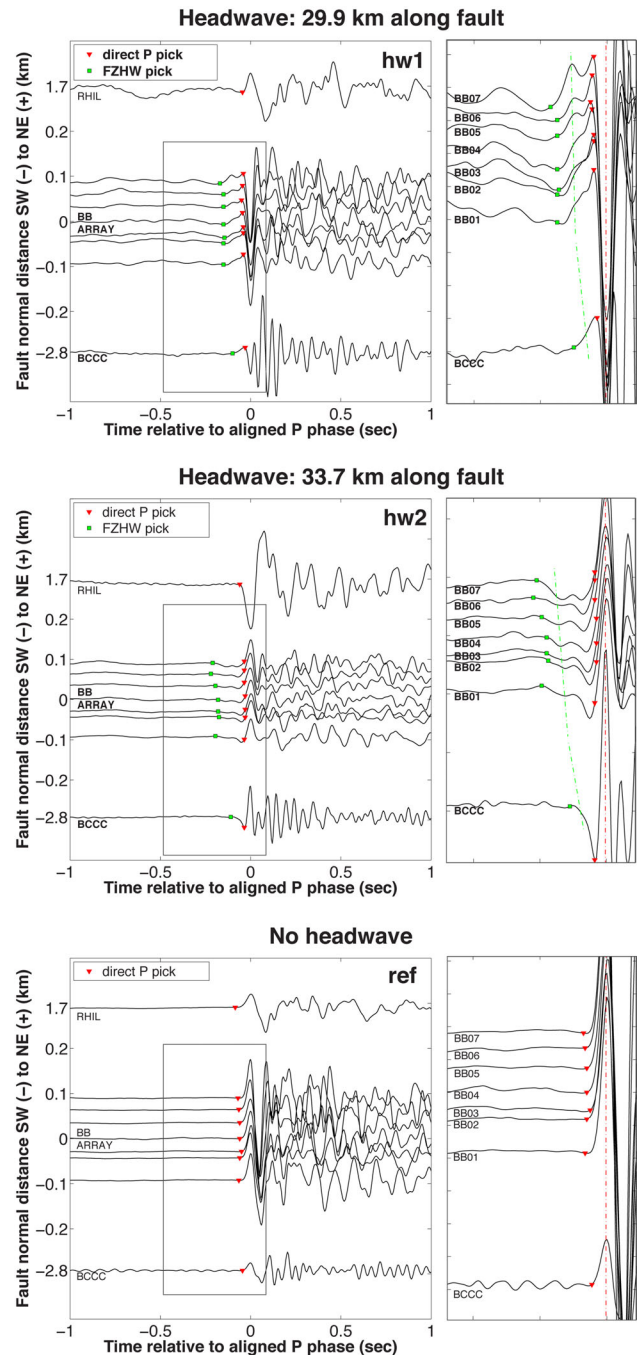

Figure 7. Comparison of displacement waveforms (vertical component) from events hw1 (top) and hw2 (middle) generating FZHW at the BB array and station BCCC and event ref (bottom) that does not generate FZHW. No FZHW are observed at station RHIL for these events. Waveforms are aligned on direct *P* phases and BB traces are normalized relative to BB01 while waveforms recorded by reference stations are normalized by themselves. Left-hand panels contain 2 s windows centred on direct *P* waves and right-hand panels are 0.55 s zooms of early *P* waveforms.

neath the array and changes in topography (Jepsen & Kennett 1990; Neuberg & Pointer 2000).

Instead of determining the onset of direct *P* waves from characteristics of the polarization ellipse a different approach is used. HPM of *P* waveforms from events generating FZHW are visually compared with those from reference events without FZHW. The
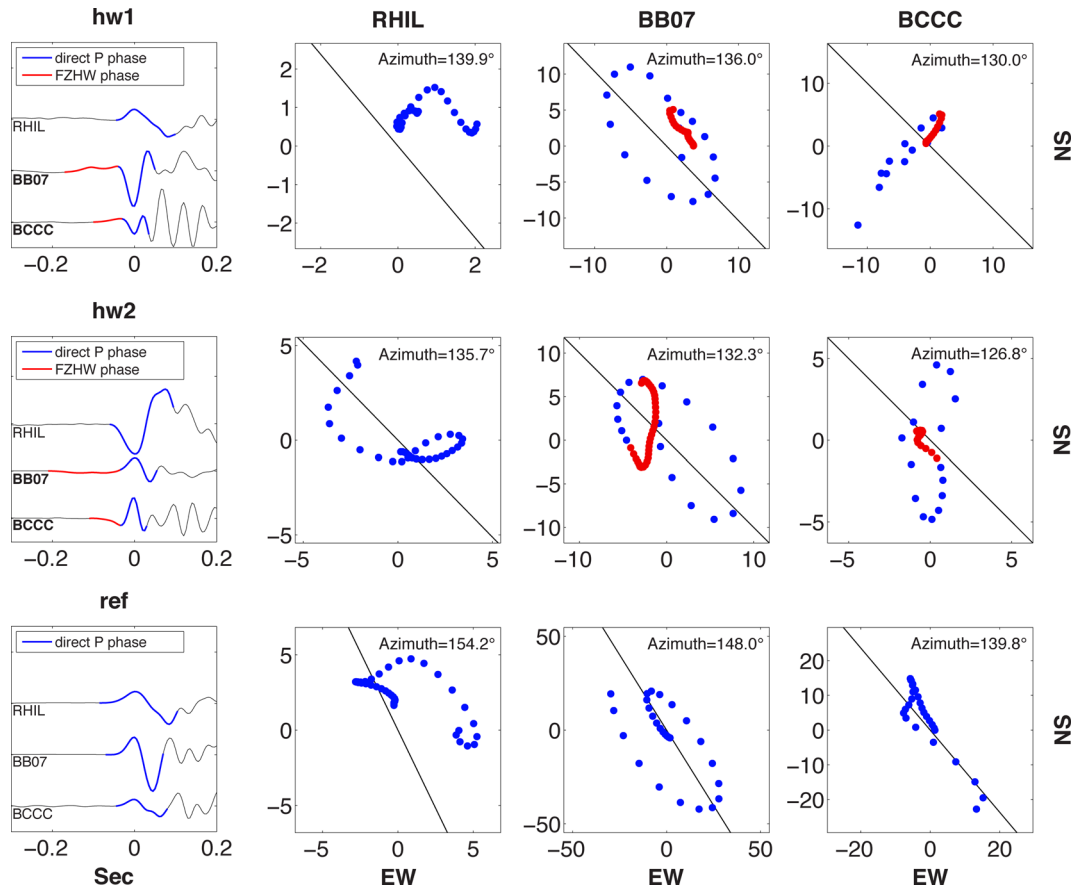
Figure 8. Horizontal particle motion (HPM) are plotted for two events, hw1 and hw2, that generated FZHW (rows 1 and 2, respectively) and a reference event, ref, that did not generate FZHW (row 3). Column 1 shows displacement *P* waveforms (vertical component) from events hw1, hw2 and ref recorded at stations RHIL, BB07 and BCCC. Direct *P* waves are highlighted in blue and FZHW are highlighted in red. Columns 2, 3 and 4 show corresponding HPM for the three events of direct *P* waves (blue dots) and FZHW (red dots) recorded at stations RHIL, BB07 and BCCC, respectively.

onset of direct *P* waves in waveforms with FZHW are chosen to be the times when HPM of those waveforms becomes most coherent with HPM of reference *P* waves. The reference events are identified with criteria opposite to those used to identify FZHW, namely: (1) FZHW are not picked for any station and 2) first arrivals are impulsive and highly coherent between stations (Fig. 7, bottom panel). The identified reference events are located closer to the recording station and/or more off fault compared to events generating FZHW. For an event generating FZHW, the reference event with the closest hypocentre and a difference in back azimuth less than 20° is used.

Fig. 8 shows a comparison based on this approach of the first 0.5 s of waveforms with FZHW to the first *P* wave wiggle of reference waveforms. HPM of traces with FZHW contain parts that are uncorrelated (red HPM, Fig. 8 rows 1 and 2) and correlated (blue HPM, Fig. 8 rows 1 and 2) with the HPM of reference traces (blue HPM, Fig. 8 row 3). Uncorrelated and correlated HPM correspond to FZHW and direct *P* waves, respectively. As can be seen, uncorrelated and correlated HPM do not necessarily point in the fault and epicentre directions, respectively. This is probably associated with the complex structure and is the case even for reference stations. Similar results are obtained for a total of 24 out the 49 candidate events (locations in Fig. 6). The direct *P* picks for those events are adjusted accordingly. Differential times Δt computed from adjusted FZHW and direct *P* picks are greatest for BB07 and decrease towards BCCC (Fig. 7 top and middle panels) for all 24 events.

Additional support for FZHW is given by the ratio of largest eigenvalues calculated for noise, FZHW and direct *P* waves. Ideally, the largest eigenvalue of a window containing a FZHW will be larger than noise, and the largest eigenvalue corresponding to a direct *P* wave would be larger still (Bulut *et al.* 2012; Allam *et al.* 2014b). Eigenvalues are computed for phases generated by the 24 events and recorded at station BB07. For each event, calculations are made for two non-overlapping time windows of length Δt (for that event), where the first sample of the second window was firstly aligned with the FZHW pick (to compare noise and FZHW) and then shifted to align with the direct *P* pick (to compare FZHW and direct *P* wave). On average, the eigenvalue ratio between windows containing FZHW and noise is 26.14 (minimum of 0.21 and maximum of 514.44), and between direct *P* wave and FZHW windows it is 27.28 (minimum of 1.99 and maximum of 85.61).

Fig. 9 shows the moveout, Δt, between the FZHW and direct *P* waves versus along-fault distance for the 24 events generating FZHW. The observed moveout is used to estimate an average velocity contrast across the Clark Fault (eq.1) in the study area. The moveout is similar for events located both northwest and southeast of the array. The obtained average velocity contrast over the propagation paths associated with the used events is ∼3.2 per cent. This estimate assumes an average *P*-wave velocity of 6.5 km/s, based on the *P* velocity of the regional 1-D model at the 16 km median depth of the 24 events. The moveout becomes constant for events located >40 km southeast of the array (Fig. 9). This can be explained
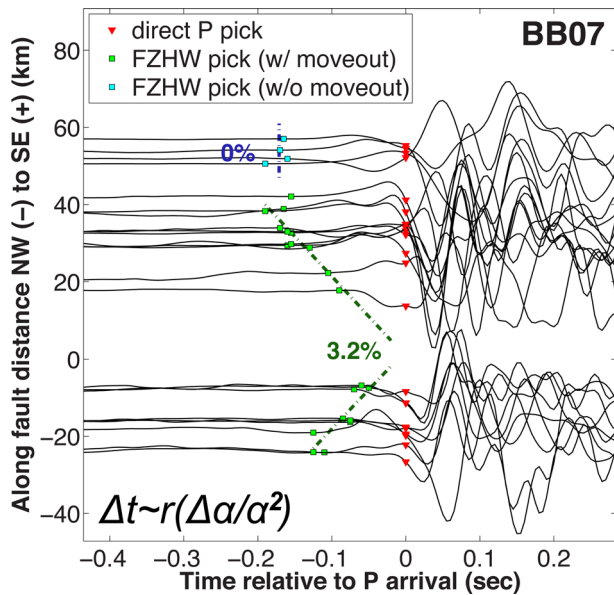
Figure 9. Displacement waveforms (vertical component) from 24 events generating FZHW at BB07 sorted by propagation distance along the fault. The linear moveout of FZHW (green lines and squares) relative to direct *P* (red triangles) arrivals from events less than ~40 km away corresponds to a 3.2 per cent average velocity contrast across the fault. The moveout is constant for events >40 km southeast of the array (cyan squares and blue line).

by these events being located more off fault at depth compared to closer events (their epicentres have largest fault normal distances, Fig. 6). Alternatively, if these events are located close to the fault the constant moveout indicates the imaged bimaterial interface is limited laterally and in depth beyond 40 km epicentral distance.

3.4 Fault zone trapped waves

3.4.1 Methodology

Relatively uniform low velocity fault damage zones can act as waveguides and generate constructive interference of *S*, *P* and noise phases giving rise to FZTW (e.g. Ben-Zion & Aki 1990; Igel *et al.* 1997, Jahnke *et al.* 2002; Hillers *et al.* 2014). These phases have been observed in various fault and geologic settings in California (Li *et al.* 1994; Peng *et al.* 2003; Lewis & Ben-Zion 2010) including the SJFZ (Li & Vernon 2001; Lewis *et al.* 2005; Qiu *et al.* 2017), Turkey (Ben-Zion *et al.* 2003), Italy (Rovelli *et al.* 2002; Calderoni *et al.* 2012; Avallone *et al.* 2014), Japan (Mizuno & Nishigami 2006) and New Zealand (Eccles *et al.* 2015).

FZTW appear on seismograms as high amplitude, long duration, low frequency phases that follow direct arrivals and are observed only at stations that are within or very close to the trapping structure (e.g. Li & Leary 1990; Ben-Zion *et al.* 2003; Lewis & Ben-Zion 2010). In this study the focus is on identifying and analysing Love-type FZTW that follow the direct *S* wave (Ben-Zion 1998). The first step in identifying events generating candidate FZTW is automatic detection (Ross & Ben-Zion 2015). The detection algorithm is based on the dominant period, wave energy, ratio between absolute peak amplitude and average amplitude, and delay between the absolute peak and *S* pick within a 1 s window starting at the *S* pick for each station. In order to minimize false detections due to site amplification, the energy in a longer 6 s window is also computed. The computations are done on vertical and fault-parallel component

velocity seismograms. An outlier detection is used to flag station(s) with calculated values for the short time windows after the direct *S* wave significantly larger than the median values of all stations. This detection method works best if the number of stations with no FZTW phases outnumber the ones with FZTW phases.

After candidate FZTW are detected they are visually inspected. Any anomalous phase flagged for a given event at only one station is discarded as a possible FZTW. This is because trapping structures are typically ~100 m wide (e.g. Li & Vernon 2001; Lewis *et al.* 2005; Qiu *et al.* 2017) so FZTW should be observed at multiple stations of the dense array. Noise components observed at a single or several stations are also sometimes flagged as possible FZTW and are discarded during visual inspection. Waveforms generated by events similar in size and within 20 km from those generating the remaining FZTW are inspected to identify additional candidates. Waveforms from events producing clear FZTW are inverted for parameters of the trapping structure, using the genetic inversion algorithm of Michael & Ben-Zion (1998) with a forward kernel based on the analytical solution of Ben-Zion & Aki (1990) and Ben-Zion (1998). This inversion process explores systematically the significant trade-offs between the key parameters governing properties of FZTW (e.g. Peng *et al.* 2003; Qiu *et al.* 2017).

3.4.2 Results

The automatic detection algorithm of Ross & Ben-Zion (2015) flagged potential FZTW within waveforms from 624 events, with 94 per cent of all detections shared between stations BB04 to BB07. The flagged waveforms are visually inspected, erroneous picks are discarded and additional FZTW phases are identified. Newly identified FZTW waveforms are only observed for stations BB04 to BB07. This procedure leads to identification of 16 events that produce high quality waveforms with FZTW (Fig. 10). All but one of the events are located north-northeast of the array and most are at considerable distance from the Clark fault (Fig. 10 left). The generation of FZTW by events at considerable distance from the fault indicates that the trapping structure extends primarily over the top few km of the crust (Ben-Zion *et al.* 2003; Fohrmann *et al.* 2004).

The velocity waveforms generated by two example events (tw1 and tw2, Fig. 10) with clear FZTW phases are pre-processed for inversion. The waveforms are corrected for the instrument response, rotated to the fault-parallel component, bandpass filtered at 2–20 Hz and integrated to displacement (Figs 11a and 12a). As a final step, the seismograms are convolved with $1/t^{1/2}$ to convert a point source response to that of an equivalent line dislocation source (e.g. Igel *et al.* 2002; Ben-Zion *et al.* 2003). The inverted model parameters are: (1–3) *S* velocities of the two quarter spaces (assumed different based on Section 3.3.2) and the fault zone layer, (4–5) width and *Q* value of the fault zone layer, (6) location of contact between the fault and left quarter space, and (7) propagation distance within the fault zone layer. Estimates of the location where energy enters the low velocity layer (virtual source) and the travel time outside this layer are derived from the seven parameters. The allowable bounds for the first six parameters and incremental changes allowed in each are shown in Table 2.

The genetic inversion algorithm maximizes the correlation between sets of observed waveforms (seven each in this study) and synthetic seismograms generated with the solution of Ben-Zion & Aki (1990) and Ben-Zion (1998), while exploring systematically a large parameter-space. This is accomplished by calculating fitness values associated with different sets of model parameters and
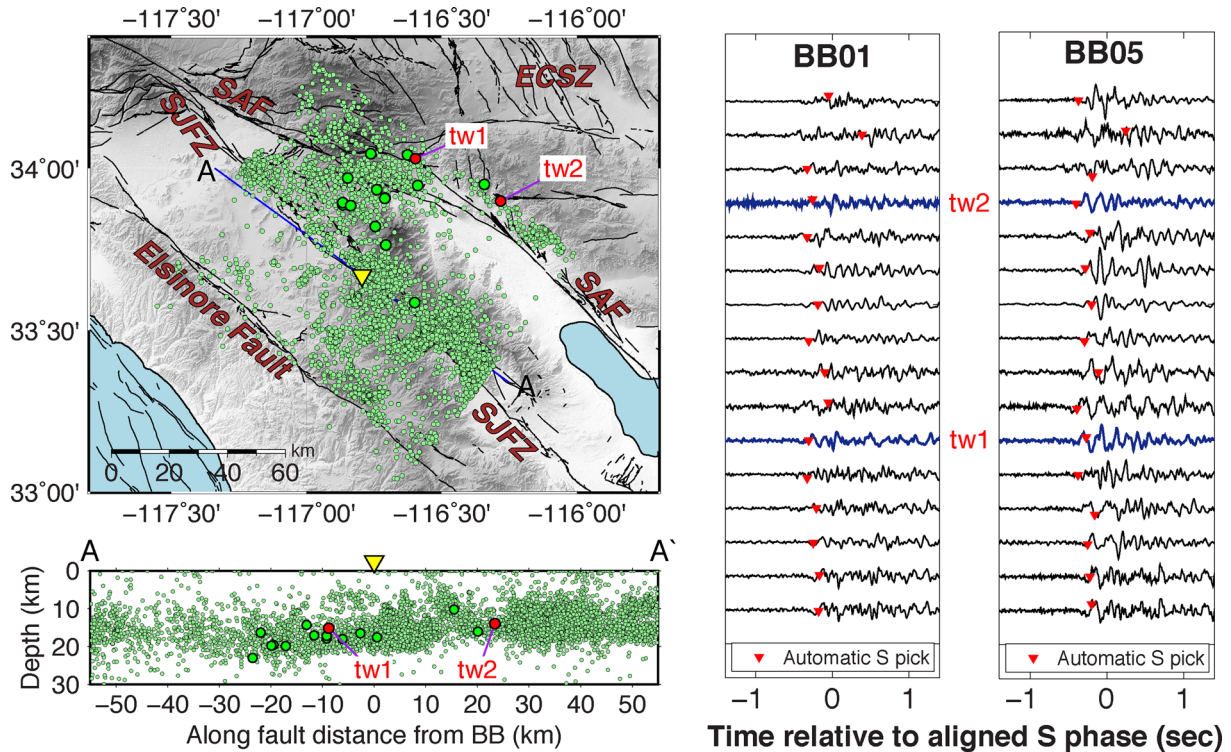
Figure 10. Locations and waveforms from events analysed during the FZTW study. (Top left) BB array (yellow triangle), all events (circles) analysed for the presence of FZTW and the 16 events (large circles) for which clear FZTW are observed. (Bottom left) A depth section of events projected along the profile A–A′ on top. (Right) Velocity waveforms (fault-parallel component) produced by the 16 events and recorded at stations BB01 and BB05. The two traces for each event are normalized by BB01. Highlighted are waveforms from two example events tw1 and tw2 (large red circles on left) used during inversion for fault zone structure.

migrating in the parameter-space overall in the direction of larger fitness values. The fitness is defined as $(1+C)/2$ where C is the cross-correlation coefficient between observed and synthetic waveforms. When C varies over the range -1 (perfect anti-correlation) to 1 (perfect correlation), the fitness value changes from 0 to 1. Fig. 11(b) shows synthetic (blue lines) waveform fits produced during 10 000 inversion iterations (testing 10 000 sets of model parameters). Fig. 11(c) displays the fitness values (dots) calculated by the inversion algorithm for the final 2000 iterations. The curves in Fig. 11(c) give probability density functions for the various model parameters, calculated by summing the fitness values of the final 2000 inversion iterations and normalizing the results to have unit sums. The model parameters associated with the highest fitness values (solid circles in Fig. 11c) are used to produce the synthetic waveform fits of Fig. 11(b).

Fig. 12 presents corresponding inversion results for the second example event. The best-fitting and most likely parameters of the trapping structure produced by inversions of waveforms generated by different events should be similar. This is the case for the results in Figs 11 and 12 and inversion results of several other high quality waveforms with FZTW. Based on the inversion results, the fault/damage zone is estimated to start beneath station BB04 (the local coordinate system is centred on BB04), extend about 130–200 m to the NE, have a Q value of 10–20, an S velocity reduction of 30–40 per cent relative to the neighbouring rock and a depth extent of 3.3–4 km. The latter range is estimated by dividing the most likely total propagation distance within the fault zone by $\sqrt{2}$ to account for a horizontal propagation component.

4 DISCUSSION

The different types of analysis presented in Section 3 can be combined to produce a detailed model for the internal structure of the SJFZ in the study area (Fig. 13). Both the local and teleseismic delay time analyses show larger slowness beneath BB07 compared to BB01. The change in slowness observed in the teleseismic data is gradual compared to the more abrupt change based on the local earthquake seismograms (compare Fig. 2d with Figs 4 and 5a). The difference can be explained by the fact that teleseismic arrivals are associated with longer wavelengths leading to smoother results. The small-scale variations of slowness based on the local P waves likely reflect local structural variations such as near surface sediments and small-scale topography.

Stations BB04-BB07 with the lowest P wave velocities record also fault zone trapped S waves so they are within the core damage zone of the fault. The broad distribution of events generating FZTW (Fig. 10) implies that the trapping structure is relatively shallow (Fohrmann *et al.* 2004). Inversions of waveforms including FZTW indicate (Figs 11 and 12) that the trapping structure extends to a depth of ∼3.5 km and has width of ∼200 m wide, Q value of 10–20 and S velocity reduction of 30–40 per cent. These parameters are similar to properties of trapping structures at other sections of the SJFZ (Lewis *et al.* 2005; Qiu *et al.* 2017), San Andreas fault at Parkfield (Lewis & Ben-Zion 2010), Karadere branch of the North Anatolian fault (Ben-Zion *et al.* 2003) and other active strike-slip faults and rupture zones. Suggestions of trapping structures at the SJFZ and other locations that extend to the bottom of the seismogenic zone (e.g. Li & Vernon 2001; Li *et al.* 2004, 2007)
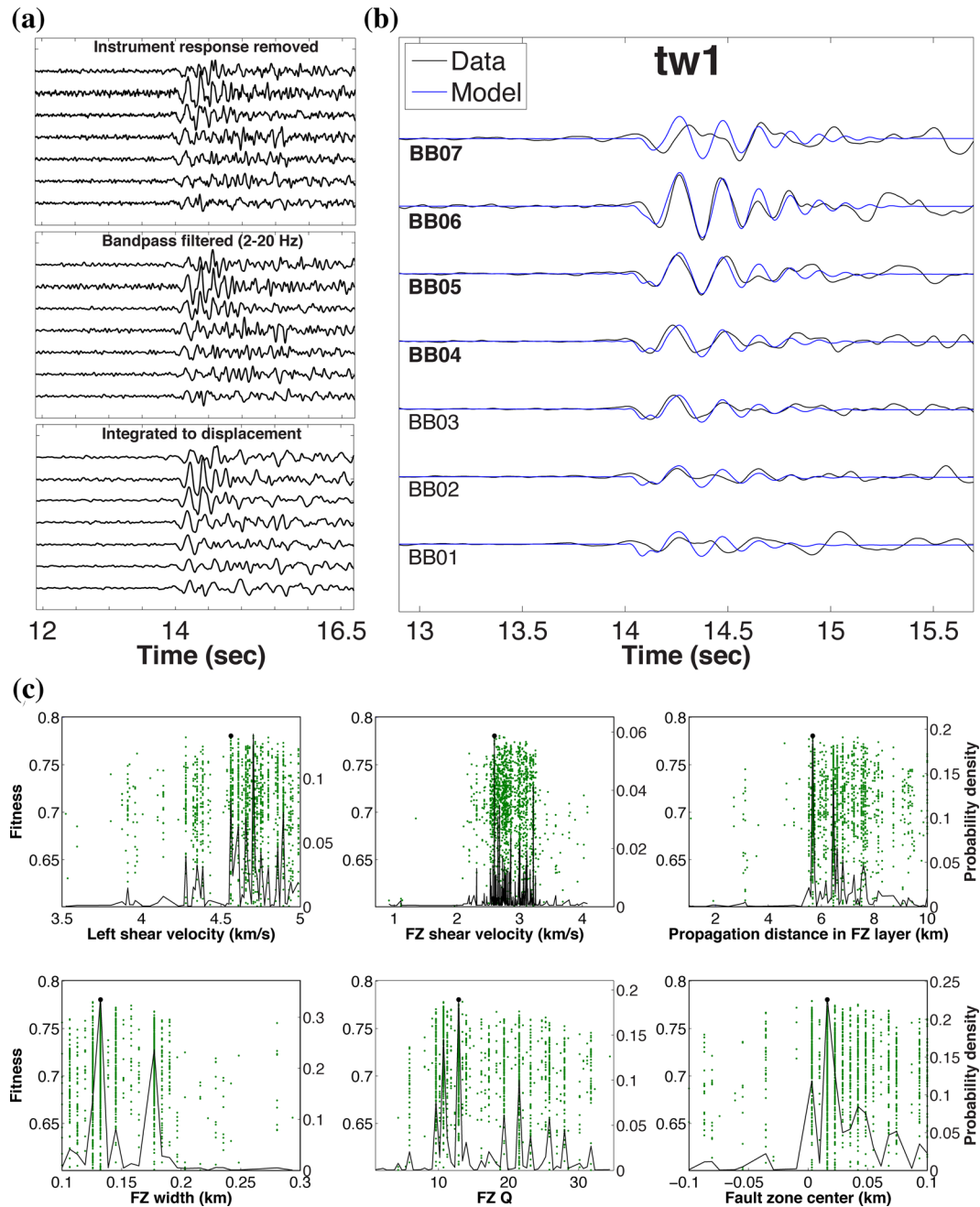
Figure 11. Fault model inversion results for event tw1. (a) Prior to inversion waveforms are deconvolved with the instrument response, band-pass filtered (2–20 Hz) and integrated to displacement. (b) Waveforms convolved with $1/t^{1/2}$ (black traces) are compared to forward modelled waveforms (blue traces) using parameters corresponding to the best-fitting solution. (c) Parameter space for the final 10 generations (2000 iterations). Green dots represent all solutions, black lines are cumulative solution density curves and black dots correspond to the best-fitting solution.

were not supported by more quantitative subsequent analyses using larger data sets (e.g. Peng *et al.* 2003; Yang & Zhu 2010).

The FZHW observed at the BB array and reference station BCCC (Fig. 7) reveal a fault bimaterial interface that extends at least ∼40 km to the southeast and to a depth of ∼20 km (depth of deepest event within 40 km generating FZHW, Fig. 6). The bimaterial interface extents also to the northwest but is more limited in space, because no events beyond ∼20 km to the northwest produce FZHW. An average *P* velocity contrast of 3.2 per cent across the interface is calculated from the moveout between the FZHW and direct *P* waves with increasing along-fault distance (Fig. 9). This contrast is not as

large as across the San Andreas fault south of Hollister (McGuire & Ben-Zion 2005), but is comparable to values obtained for the San Andreas fault around San Gorgonio Pass (Share & Ben-Zion 2016), Hayward fault (Allam *et al.* 2014b) and North Anatolian fault (Najdahmadi *et al.* 2016). The obtained value reflects an average velocity contrast over the top 20 km of the crust. The velocity contrast typically decreases with depth (Ben-Zion *et al.* 1992; Lewis *et al.* 2007), so the contrast may be double in the uppermost 7.5 km or so of the crust.

The existence of FZHW at reference station BCCC and not at station RHIL implies slower regional structure southwest of BB07 than
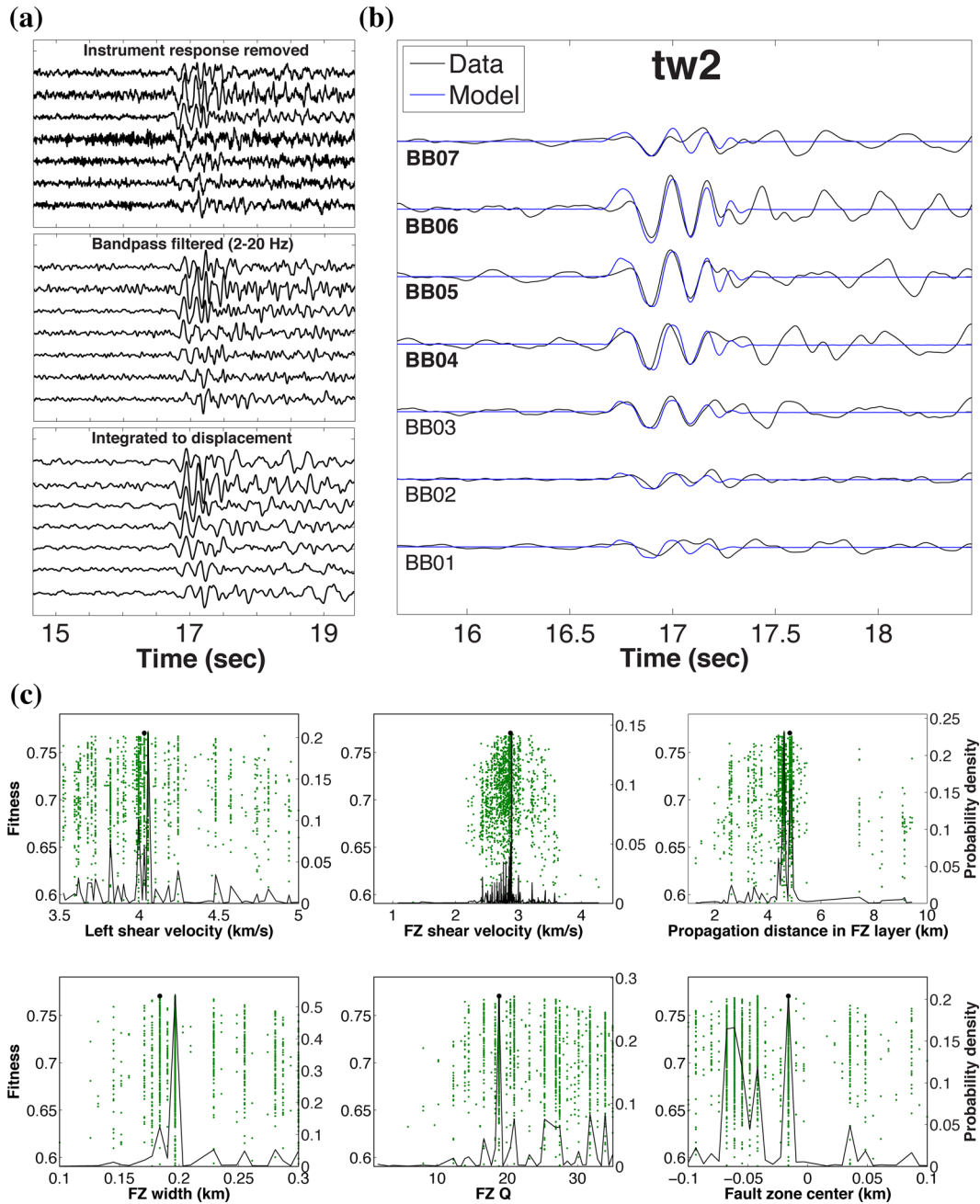
Figure 12. Fault model inversion results for event tw2. The layout and steps are the same as Fig. 11.

northeast of it. This is consistent with tomographic results for the SJFZ region based on local earthquakes and ambient seismic noise (Allam & Ben-Zion 2012; Zigone *et al.* 2015; Fang *et al.* 2016). The inferred contrast is also consistent with the surface geology, showing pre mid-Cretaceous banded gneisses on the southwest side of the fault juxtaposed against mid-Cretaceous tonalitic rocks on the northeast (Sharp 1967). The tomographic results show a reversal in the sense of velocity contrast across the Clark Fault to the northwest of the array, which explains the lack of FZHW from events farther than ~20 km in that direction. The bimaterial interface is closest to BB07 because the moveout between the head and direct *P* waves decreases from that station. The region beneath BB04–BB07 has low *P* velocities based on the teleseismic and local delay times (Figs 2d, 4 and 5a) and acts as a trapping structure for *S* waves (Figs 11 and

12). Based on the results from the different data sets and analyses, the head waves propagate along a bimaterial interface that is at the edge of the core damage zone in the top few km and merges with the main Clark fault at depth (Fig. 13). The best available geological data places the main Clark fault trace directly beneath BB04. The trapping structure and zone with largest delay times exist primarily in the crustal block with faster seismic velocity at depth.

The sense of velocity contrast across the Clark fault at depth and theoretical results on bimaterial ruptures (e.g. Weertman 1980; Ben-Zion & Andrews 1998; Ampuero & Ben-Zion 2008; Brietzke *et al.* 2009) suggest that earthquakes in the area tend to propagate to the northwest. This is consistent with observed directivities of small to moderate events on the section southeast of the array (Kurzon *et al.* 2014; Ross & Ben-Zion 2016), along-strike

Table 2. Upper and lower bounds placed on, and incremental change allowed in, the parameter space during inversions of events tw1 and tw2 (Figs 11 and 12). Density is fixed at 2.5 g cm^{-3} during inversion. FZ, fault zone; QS, quarter space; S, shear; Q, quality factor and FZ centre is the contact between the left QS and FZ layer.

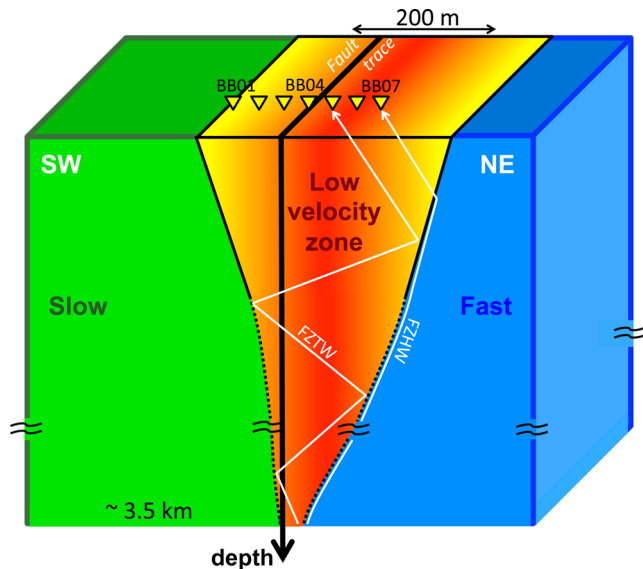| Parameter	Lower bound	Upper bound	Increment
FZ S velocity	0.7 (km s^{-1})	4.5 (km s^{-1})	0.1 (km s^{-1})
Left QS S velocity	3.5 (km s^{-1})	5.0 (km s^{-1})	0.2 (km s^{-1})
Right QS S velocity	3.15 km s^{-1}	5.5 (km s^{-1})	0.2 (km s^{-1})
FZ Q	1	35	1
Left QS Q	200	200	Fixed
Right QS Q	200	200	Fixed
FZ centre	−100 m	100 m	10 m
FZ width	100 m	300 m	10 m

Figure 13. Conceptual model for the Clark fault at Blackburn Saddle based on results presented here.

asymmetry of aftershocks in the area (Zaliapin & Ben-Zion 2011) and small reversed-polarity deformation structures in the Hemet stepover region to the northwest (Ben-Zion *et al.* 2012). Persistent occurrence of bimaterial ruptures with preferred propagation direction is expected to produce more damage on the side with faster velocity at depth (Ben-Zion & Shi 2005). This is in agreement with the observations summarized in Fig. 13 and geological mapping near Hog Lake southeast of the array (Dor *et al.* 2006).

Stations at larger distance from the fault may record, in addition to the phases analysed in this work, also *P* and *S* body waves reflected within a low velocity fault zone layer (Yang *et al.* 2014) and waves reflected from bimaterial fault interfaces to off-fault stations (Najdahmadi *et al.* 2016). A recent deployment of a longer aperture array across the Clark fault at the same location of the BB array (Lin *et al.* 2016) provides opportunities for analysing these and other signals indicative of the inner structure of the fault. This will be done in a follow up work.

ACKNOWLEDGEMENTS

REFERENCES

Allam, A. & Ben-Zion, Y., 2012. Seismic velocity structures in the southern California plate boundary environment from double difference tomography, *Geophys. J. Int.,* **190,** 1181–1196.

Allam, A.A., Ben-Zion, Y., Kurzon, I. & Vernon, F., 2014a. Seismic velocity structure in the Hot Springs and Trifurcation areas of the San Jacinto fault zone, California, from double-difference tomography, *Geophys. J. Int.,* **198,** 978–999.

Allam, A.A., Ben-Zion, Y. & Peng, Z., 2014b. Seismic imaging of a bimaterial interface along the Hayward fault, CA, with fault zone head waves and Direct P arrivals, *Pure appl. Geophys.,* **171**(11), 2993–3011.

Ampuero, J.P. & Ben-Zion, Y., 2008. Cracks, pulses and macroscopic asymmetry of dynamic rupture on a bimaterial interface with velocity-weakening friction, *Geophys. J. Int.,* **173**(2), 674–692.

Andrews, D.J. & Ben-Zion, Y., 1997. Wrinkle-like slip pulse on a fault between different materials, *J. geophys. Res.,* **102,** 553–571.

Avallone, A., Rovelli, A., Di Giulio, G., Improta, L., Ben-Zion, Y., Milana, G. & Cara, F., 2014. Waveguide effects in very high rate GPS record of the 6 April 2009, Mw 6.1 L'Aquila, central Italy earthquake, *J. geophys. Res.,* **119,** 490–501.

Bailey, I.W., Ben-Zion, Y., Becker, T.W. & Holschneider, M., 2010. Quantifying focal mechanism heterogeneity for fault zones in central and southern California, *Geophys. J. Int.,* **183**(1), 433–450.

Bennington, N.L., Thurber, C., Peng, Z., Zhang, H. & Zhao, P., 2013. Incorporating fault zone head wave and direct wave secondary arrival times into seismic tomography: application at Parkfield, California, *J. geophys. Res.,* **118,** 1008–1014.

Ben-Zion, Y., 1989. The response of two joined quarter spaces to SH line sources located at the material discontinuity interface, *Geophys. J. Int.,* **98,** 213–222.

Ben-Zion, Y., 1998. Properties of seismic fault zone waves and their utility for imaging low-velocity structures, *J. geophys. Res.,* **103,** 12567–12585.

Ben-Zion, Y., 1990. The response of two half spaces to point dislocations at the material interface, *Geophys. J. Int.,* **101,** 507–528.

Ben-Zion, Y. & Aki, K., 1990. Seismic radiation from an SH line source in a laterally heterogeneous planar fault zone, *Bull. seism. Soc. Am.,* **80,** 971–994.

Ben-Zion, Y. & Andrews, D.J., 1998. Properties and implications of dynamic rupture along a material interface, *Bull. seism. Soc. Am.,* **88**(4), 1085–1094.

Ben-Zion, Y. & Malin, P., 1991. San Andreas fault zone head waves near Parkfield, California, *Science,* **251,** 1592–1594.

Ben-Zion, Y. & Shi, Z., 2005. Dynamic rupture on a material interface with spontaneous generation of plastic strain in the bulk, *Earth planet. Sci. Lett.,* **236**(1), 486–496.

Ben-Zion, Y., Katz, S. & Leary, P., 1992. Joint inversion of fault zone head waves and direct P arrivals for crustal structure near major faults, *J. geophys. Res.,* **97,** 1943–1951.

Ben-Zion, Y. *et al.*, 2003. A shallow fault-zone structure illuminated by trapped waves in the Karadere–Duzce branch of the North Anatolian Fault, western Turkey, *Geophys. J. Int.,* **152**(3), 699–717.

Ben-Zion, Y., Rockwell, T., Shi, Z. & Xu, S., 2012. Reversed-polarity secondary deformation structures near fault stepovers, *J. appl. Mech.,* **79,** 031025, doi: 10.1115/1.4006154.

Ben-Zion, Y. *et al.*, 2015. Basic data features and results from a spatially dense seismic array on the San Jacinto fault zone, *Geophys. J. Int.,* **202,** 370–380.

Brietzke, G.B., Cochard, A. & Igel, H., 2009. Importance of bimaterial interfaces for earthquake dynamics and strong ground motion, *Geophys. J. Int.,* **178,** 921–938.

Bulut, F., Ben-Zion, Y. & Bonhoff, M., 2012. Evidence for a bimaterial interface along the Mudurnu segment of the North Anatolian Fault Zone from polarization analysis of P waves, *Earth planet. Sci. Lett.,* **327-328,** 17–22.

Calderoni, G., Di Giovambattista, R., Vannoli, P., Pucillo, S. & Rovelli, A., 2012. Fault-trapped waves depict continuity of the fault system responsible for the 6 April 2009 M$_W$ 6.3 L'Aquila earthquake, central Italy, *Earth planet. Sci. Lett.,* **323-324,** 1–8.

Crotwell, H.P., Owens, T.J. & Ritsema, J., 1999. The TauP Toolkit: Flexible seismic travel-time and ray-path utilities, *Seismol. Res. Lett.,* **70**(2), 154–160.

Dor, O., Rockwell, T.K. & Ben-Zion, Y., 2006. Geological observations of damage asymmetry in the structure of the san jacinto, san andreas and punchbowl faults in southern california: a possible indicator for preferred rupture propagation direction, *Pure appl. Geophys.,* **163,** 301–349.

Dor, O., Yildirim, C., Rockwell, T.K., Ben-Zion, Y., Emre, O., Sisk, M. & Duman, T.Y., 2008. Geological and geomorphologic asymmetry across the rupture zones of the 1943 and 1944 earthquakes on the North Anatolian Fault: possible signals for preferred earthquake propagation Direction, *Geophys. J. Int.,* **173,** 483–504.

Eccles, J.D., Gulley, A.K., Malin, P.E., Boese, C.M., Townend, J. & Sutherland, R., 2015. Fault Zone Guided Wave generation on the locked, late interseismic Alpine Fault, New Zealand, *Geophys. Res. Lett.,* **42**(14), 5736–5743.

Ellsworth, W.L. & Malin, P.E., 2011. Deep rock damage in the San Andreas Fault revealed by P-and S-type fault-zone-guided waves, *Geol Soc, Lond, Special Publications,* **359**(1), pp.39–53.

Fang, H., Zhang, H., Yao, H., Allam, A., Zigone, D., Ben-Zion, Y., Thurber, C. & van der Hilst, R.D., 2016. A new three-dimensional joint inversion algorithm of body-wave and surface-wave data and its application to the Southern California Plate Boundary Region, *J. geophys. Res.,* **121,** 3557–3569.

Fialko, Y., 2006. Interseismic strain accumulation and the earthquake potential on the southern San Andreas fault system, *Nature,* **441,** 968–971.

Fohrmann, M., Igel, H., Jahnke, G. & Ben-Zion, Y., 2004. Guided waves from sources outside faults: an indication for shallow fault zone structure?, *Pure appl. Geophys.,* **161,** 2125–2137.

Hauksson, E., Yang, W. & Shearer, P.M., 2012. Waveform relocated earthquake catalog for southern California (1981 to June 2011), *Bull. seism. Soc. Am.,* **102**(5), 2239–2244.

Hillers, G., Campillo, M., Ben-Zion, Y. & Roux, P., 2014. Seismic fault zone trapped noise, *J. geophys. Res.,* **119**(7), 5786–5799.

Hillers, G., Roux, P., Campillo, M. & Ben-Zion, Y., 2016. Focal spot imaging based on zero lag cross correlation amplitude fields: Application to dense array data at the San Jacinto fault zone, *J. geophys. Res.,* **121,** doi:10.1002/2016JB013014.

Igel, H., Ben-Zion, Y. & Leary, P., 1997. Simulation of SH and P SV wave propagation in fault zones, *Geophys. J. Int.,* **128,** 533–546.

Igel, H., Jahnke, G. & Ben-Zion, Y., 2002. Numerical simulation of fault zone guided waves: accuracy and 3-D effects, *Pure appl. Geophys.,* **159,** 2967–2083.

Jahnke, G., Igel, H. & Ben-Zion, Y., 2002. Three-dimensional calculations of fault zone guided waves in various irregular structures, *Geophys. J. Int.,* **151,** 416–426.

Jepsen, D.C. & Kennett, B.L.N., 1990. Three component analysis of regional seismograms, *Bull. seism. Soc. Am.,* **80,** 2032–2052.

Johnson, H.O., Agnew, D.C. & Wyatt, F.K., 1994. Present-day crustal deformation in southern California, *J. geophys. Res.,* **99**(B12), 23951–23974.

Kurzon, I., Vernon, F.L., Ben-Zion, Y. & Atkinson, G., 2014. Ground motion prediction equations in the San Jacinto Fault Zone—significant effects of rupture directivity and fault zone amplification, *Pure appl. Geophys.,* **171,** 3045–3081.

Lewis, M.A. & Ben-Zion, Y., 2010. Diversity of fault zone damage and trapping structures in the Parkfield section of the San Andreas Fault from comprehensive analysis of near fault seismograms, *Geophys. J. Int.,* **183**(3), 1579–1595.

Lewis, M.A., Peng, Z., Ben-Zion, Y. & Vernon, F.L., 2005. Shallow seismic trapping structure in the San Jacinto fault zone near Anza, California, *Geophys. J. Int.,* **162,** 867–881.

Lewis, M.A., Ben-Zion, Y. & McGuire, J., 2007. Imaging the deep structure of the San Andreas Fault south of Hollister with joint analysis of fault-zone head and Direct P arrivals, *Geophys. J. Int.,* **169,** 1028–1042.

Li, Y.-G. & Leary, P.C., 1990. Fault zone trapped seismic waves, *Bull. seism. Soc. Am.,* **80**(5), 1245–1271.

Li, Y.-G. & Vernon, F.L., 2001. Characterization of the San Jacinto fault zone near Anza, California, by fault zone trapped waves, *J. geophys. Res.,* **106,** 30671–30688.

Li, Y.-G., Aki, K., Adams, D., Hasemi, A. & Lee, W.H.K., 1994. Seismic guided waves trapped in the fault zone of the Landers, California, earthquake of 1992, *J. Res. geophys,* **99,** 11705–11722.

Li, Y.-G., Vidale, J.E. & Cochran, E.S., 2004. Low-velocity damaged structure of the San Andreas Fault at Parkfield from fault zone trapped waves, *Geophys. Res. Lett.,* **31,** L12S06.

Li, Y.-G., Chen, P., Cochran, E.S. & Vidale, J.E., 2007. Seismic velocity variations on the San Andreas fault caused by the 2004 *M*6 Parkfield Earthquake and their implications, *Earth planets and Space,* **59**(1), 11705–11722.

Li, Z., Peng, Z., Ben-Zion, Y. & Vernon, F.L., 2015. Spatial variations of shear-wave anisotropy near the San Jacinto Fault Zone in Southern California, *J. Res. geophys,* **120,** 8334–8347.

Lin, F.-C., Allam, A.A., Share, P.-E., Ben-Zion, Y., Vernon, F., Schuster, G.T. & Karplus, M.S., 2016. Constraints on fault damage zone properties and normal modes from a dense linear array deployment along the San Jacinto Fault Zone, *Abstract S43B-2849 presented at 2016 Fall Meeting,* AGU, San Francisco, CA, 12–16 Dec.

Lindsey, E.O., Sahakian, V.J., Fialko, Y., Bock, Y., Barbot, S. & Rockwell, T.K., 2014. Interseismic Strain Location in the San Jacinto Fault Zone, *Pure appl. Geophys.,* **171,** 2937–2954.

McGuire, J. & Ben-Zion, Y., 2005. High-resolution imaging of the Bear Valley section of the San Andreas Fault at seismogenic depths with fault-zone head waves and relocated seismicity, *Geophys. J. Int.,* **163,** 152–164.

McNally, K.C. & McEvilly, T.V., 1977. Velocity contrast across the San Andreas fault in central California: small-scale variations from P-wave nodal plane distortion, *Bull. seism. Soc. Am.,* **67,** 1565–1576.

Michael, A.J. & Ben-Zion, Y., 1998. Inverting fault zone trapped waves with genetic algorithm, *EOS, Trans. A m. geophys. Un.,* 79, F584.

Mizuno, T. & Nishigami, K., 2006. Deep structure of the Nojima fault, southwest Japan, estimated from borehole observation of fault-zone trapped waves, *Tectonophysics,* **417,** 231–247.

Najdahmadi, B., Bohnhoff, M. & Ben-Zion, Y., 2016. Bimaterial interfaces at the Karadere segment of the North Anatolian Fault, northwestern Turkey, *J. geophys. Res.,* **121,** 931–950.

Neuberg, J. & Pointer, T., 2000. Effects of volcano topography on seismic broad-band waveforms, *Geophys. J. Int.,* **143,** 239–248.

Oppenheimer, D.H., Reasenberg, P.A. & Simpson, R.W., 1988. Fault plane solutions for the 1984 Morgan Hill, California, earthquake sequence: evidence for the state of stress on the Calaveras fault, *J. geophys. Res.,* **93,** 9007–9026.

Peng, Z., Ben-Zion, Y., Michael, A.J & Zhu, L.P., 2003. Quantitative analysis of seismic fault zone waves in the rupture zone of the Landers, 1992, California earthquake: evidence for a shallow trapping structure, *Geophys. J. Int.,* **155,** 1021–1041.

Qiu, H., Ben-Zion, Y., Ross, Z.E., Share, P-E. & Vernon, F., 2017. Internal structure of the San Jacinto fault zone at Jackass Flat from data recorded by a dense linear array, *Geophys. J. Int.,* **209,** 1369–1388.

Rockwell, T.K., Dawson, T.E., Ben-Horin, J.Y. & Seitz, G., 2015. A 21-Event, 4,000-year history of surface ruptures in the Anza Seismic Gap, San Jacinto Fault, and implications for long-term earthquake production on a major plate boundary fault, *Pure appl. Geophys.,* **172**(5), 1143–1165.

Ross, Z.E. & Ben-Zion, Y., 2014. Automatic picking of Direct P, S seismic phases and fault zone head waves, *Geophys. J. Int.,* **199,** 368–381.

Ross, Z.E. & Ben-Zion, Y., 2015. An algorithm for automated identification of fault zone trapped waves, *Geophys. J. Int.,* **202,** 933–942.

Ross, Z.E. & Ben-Zion, Y., 2016. Toward reliable automated estimates of earthquake source properties from body wave spectra, *J. geophys. Res.,* **121,** doi:10.1002/2016JB013003.

Rovelli, A., Caserta, A., Marra, F. & Ruggiero, V., 2002. Can seismic waves be trapped inside an inactive fault zone? The case study of Nocera Umbra, Central Italy, *Bull. seism. Soc. Am.,* **92,** 2217–2232.

Salisbury, J.B., Rockwell, T.K., Middleton, T.J. & Hudnut, K.W., 2012. LiDAR and field observations of slip distribution for the most recent surface ruptures along the central San Jacinto Fault, *Bull. seism. Soc. Am.,* **102**(2), 598–619.

Sanders, C. & Magistrale, H., 1997. Segmentation of the northern San Jacinto fault zone, southern California, *J. geophys. Res.,* **102**(B12), 27453–27467.

Sanders, C.O. & Kanamori, H., 1984. A seismotectonic analysis of the Anza seismic gap, San Jacinto fault zone, southern California, *J. geophys. Res.,* **89**(B7), 5873–5890.

SCEDC, 2013. Southern California Earthquake Data Center. Caltech. Dataset. doi:10.7909/C3WD3xH.

Share, P.-E. & Ben-Zion, Y., 2016. Bimaterial interfaces in the South San Andreas Fault with opposite velocity contrasts NW and SE from San Gorgonio Pass, *Geophys. Res. Lett.,* **43,** doi:10.1002/2016GL070774.

Sharp, R.V., 1967. San Jacinto Fault Zone in the Peninsular Ranges of Southern California, *Geol. Soc. Am. Bull.,* **78**(6), 705–730.

Shlomai, H. & Fineberg, J., 2016. The structure of slip-pulses and supershear ruptures driving slip in bimaterial friction, *Nat. Commun.,* **7,** 11787.

Vernon, F. & Ben-Zion, Y., 2010. San Jacinto Fault Zone Experiment. International Federation of Digital Seismograph Networks. Other/Seismic Network. doi:10.7914/SN/YN_2010.

Wechsler, N., Rockwell, T.K. & Ben-Zion, Y., 2009. Application of high resolution DEM data to detect rock damage from geomorphic signals along the central San Jacinto Fault, *Geomorphology,* **113,** 82–96.

Weertman, J., 1980. Unstable slippage across a fault that separates elastic media of different elastic constants, *J. geophys. Res.,* **85,** 1455–1461.

White, M.C.A., Ross, Z.E., Vernon, F.L. & Ben-Zion, Y., 2016. A detailed automatic 1998- 2015 earthquake catalog of the San Jacinto fault zone region, Abstract of the annual meeting of the Southern California Earthquake Center.

Yang, H. & Zhu, L., 2010. Shallow low-velocity zone of the San Jacinto Fault from local earthquake waveform modelling, *Geophys. J. Int.,* **183,** 421–432.

Yang, H., Li, Z., Peng, Z., Ben-Zion, Y. & Vernon, F., 2014. Low velocity zones along the San Jacinto Fault, Southern California, from body waves recorded in dense linear arrays, *J. geophys. Res.,* **119,** 8976–8990.

Zaliapin, I. & Ben-Zion, Y., 2011. Asymmetric distribution of aftershocks on large faults in California, *Geophys. J. Int.,* **185,** 1288–1304.

Zigone, D., Ben-Zion, Y., Campillo, M. & Roux, P., 2015. Seismic tomography of the Southern California plate boundary region from noise-based Rayleigh and Love Waves, *Pure appl. Geophys.,* **172,** 1002–1032.